ELSEVIER

Microelectronics Journal 30 (1999) 1043–1056

Microelectronics Journal

www.elsevier.com/locate/mejo

Invited Paper

Mid-infrared interband cascade lasers based on type-II heterostructures

R.Q. Yang*

US Army Research Laboratory, 2800 Powder Mill Road, Adelphi, MD 20783-1197, USA

Received 20 February 1999; accepted 3 March 1999

Abstract

Interband cascade lasers take advantage of the broken-gap band alignment in type-II InAs/Ga(In)Sb heterostructures to reuse electrons for sequential photon emissions from successively connected active regions; thus, they represent a new type of mid-IR light source. The mid-IR interband cascade lasers have recently been demonstrated with large peak optical output powers (~ 0.5 W/facet), high differential external quantum efficiency (> 200%), and near-room-temperature operation (286 K). Also, emission wavelength from interband cascade light-emitting diodes has been extended to as long as 15 μm; thus verifying the unique capability of this Sb-family type-II heterostructure system to be tailored over a wide spectral range. In this work, the explorations toward the demonstration and improvement of these interband cascade lasers will be reviewed. The features and issues related to the design and modeling of the interband cascade lasers will also be discussed in connection with device performance.

Keywords: Interband cascade lasers; Type-II heterostructures; Mid-infrared

1. Introduction

Compact, reliable mid-infrared (IR) (wavelength $\lambda >$ 2.5 μm) light sources are in growing demand for commercial and military applications such as chemical sensing, infrared countermeasures (IRCM), IR illumination, IR communications, laser surgery, industrial process control, and IR radar for aircraft and automobiles. If efficient semiconductor lasers were available for the mid-IR wavelength range, they would offer considerable advantages in terms of cost, volume, weight, simplicity of design, reliability, and overall performance. Requirements for such lasers include a relatively high output power and operation either at ambient temperature or at temperatures accessible with a thermoelectric cooler. Conventionally, three narrow band gap material systems—i.e. the IV–VI lead salts, the II–VI ternary alloys, and the Sb-based III–V compounds—are employed for such long wavelength IR emitters. Of these, only the lead salt diode lasers are commercially available. However, the poor quality of these narrow band gap materials and some inherent mechanisms have limited their performance. The demonstration of a quantum cascade (QC) laser [1], based on intersubband transitions in artificial semiconductor quantum-well (QW) [2–4] structures, opened a new door toward efficient mid-IR light sources. A distinct feature of the intersubband QC laser is that injected electrons are reused, and they can generate additional photons as they cascade down each stage of the energy staircase. The recent progress [5–7] in room-temperature, high-power, and distributed-feedback QC lasers has shown the great potential of the QC configuration.

Alternatively, interband cascade (IC) lasers, utilizing optical transitions between an electron state in the conduction band and a hole state in the valence band in a staircase of Sb-based type-II QW structures as I originally proposed [8–11], represent another new class of semiconductor mid-IR light sources. The advantages of cascade injection and emission wavelength tailoring are retained in IC lasers by making use of the broken-gap band edge alignment in type-II heteostructures. As a consequence of sticking to the interband transition, the fast phonon scattering loss and polarization selection rule constraint of the intersubband QC laser are circumvented. In addition, the Auger recombination, which is the dominant source of nonradiative loss in the conventional type-I interband mid-IR lasers, can be suppressed in type-II QWs with band structure engineering. Therefore, it is possible to significantly lower the threshold current density in interband cascade lasers, and this can lead to much improved devices for a wide range of applications. The concept of type-II IC lasers is flexible, and many variations on the cascade configuration are possible [8–14]. A schematic band diagram of a typical type-II IC laser structure is shown in Fig. 1, where the valence band edge of the

* Tel.: + 1-301-394-5752; fax: + 1-301-394-2103.
E-mail address: ar107@intr.net (R.Q. Yang)

0026-2692/99/$ - see front matter
PII: S0026-2692(99)00061-0

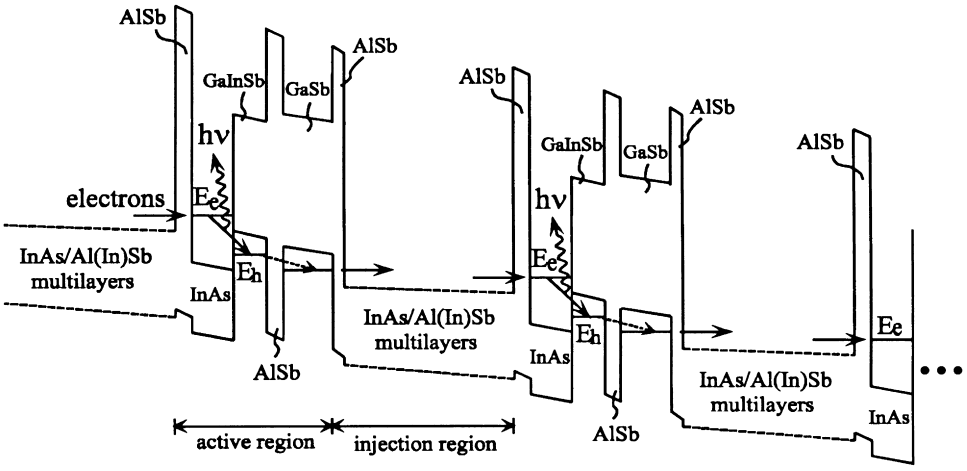

Fig. 1. Schematic band diagram of a type-II interband cascade laser structure.

Ga(In)Sb layer is higher in energy than the conduction band edge of the adjacent InAs layers, a unique feature of the natural band edge alignment in type-II broken-gap heterostructures. Here, we will focus on a few IC laser structures that have been implemented and review the explorations toward the demonstration and improvement of these IC lasers. The features and issues related to the design and modeling of the IC lasers will be discussed in connection with device performance.

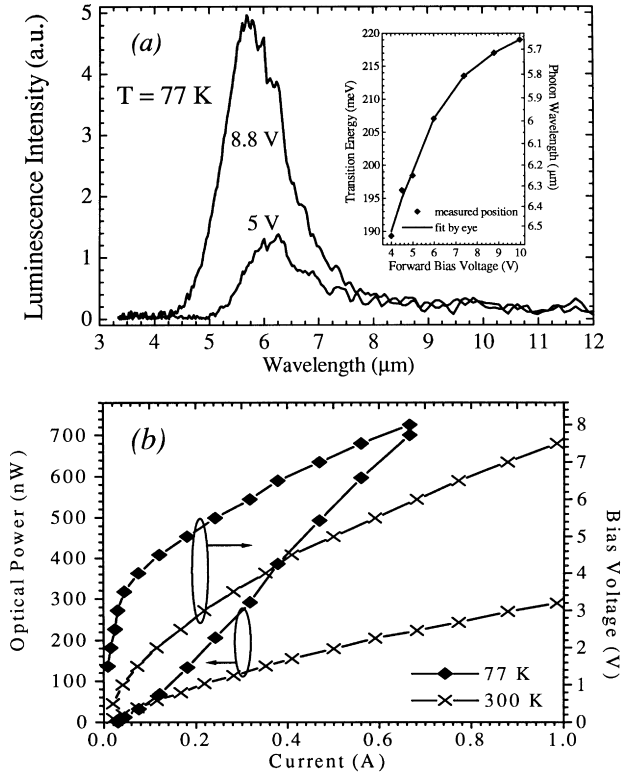

Fig. 2. (a) Electroluminescence spectra for forward bias voltages of 5 V and 8.8 V. Inset: Interband transition energy as a function of applied bias. (b) The output optical power-current and the current–voltage characteristics. The measured power was corrected only for the known losses due to reflection by the lens and dewar window, but not for the finite collection cone solid angle.

2. Early studies of IC devices

The initial experimental investigations of an InAs/AlSb/GaSb type-II IC device led to the first observation of cascade electroluminescence (EL) up to room temperature in the mid-IR spectrum (3.6–4.1 μm) [15]. The optical output power from this IC device depends weakly on temperature, suggesting that the Auger recombination processes, which are usually strongly temperature dependent, might be suppressed in type-II QW structures. However, the material quality was not good and, thus, Shockley–Read recombination might dominate in the whole temperature range. Shortly thereafter, interband cascade devices emitting at longer wavelengths (5–8 μm) were demonstrated with more detailed characterization of device performance [16,17]. Again, the optical output power was found weakly dependent on the temperature. A sizeable blue shift of the EL spectrum with the increase of the bias voltage was observed (Fig. 2) in good agreement with the theoretical calculations concerning the Stark effect on the electron and hole states in type-II QWs. A substantial change of the slope in the current–voltage (I–V) curve was also observed (Fig. 2), and indicated the near-alignment of energy levels in the injection region as suggested by the design. These investigations verified some characteristics of type-II IC structures as expected in theory and encouraged further explorations of type-II IC devices.

Subsequently, the IC laser based on InAs/GaInSb/AlSb type-II QW structures was first demonstrated at temperatures up to 170 K in early 1997 [18]. This type-II IC laser, grown in a Riber 32 MBE system on a p-type GaSb substrate, comprises 20 repeated periods of active regions separated by n-type doped injection regions as shown in Fig.

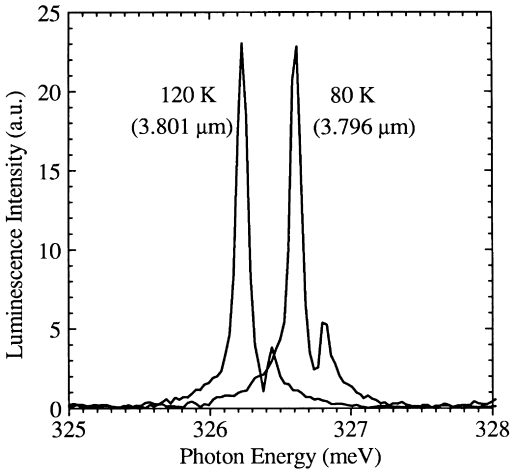

Fig. 3. Lasing spectra of the first type-II interband cascade laser at 80 and 120 K with a 0.01% duty cycle.

1. The active region comprises coupled QWs, stacked sequentially with 23 Å AlSb, 25.5 Å InAs, 34 Å $Ga_{0.7}In_{0.3}Sb$, 15 Å AlSb, and 53 Å GaSb layers. Under a forward bias, electrons are injected from the emitter into the E_e level that is in the band gap region of the adjacent GaInSb layer. As the electrons at the E_e level are effectively blocked from directly tunneling out by the GaInSb, AlSb, and GaSb layers, they tend to relax to the E_h hole state in the adjacent valence-band QW, which results in the emission of photons. Electrons at the E_h state cross the thin AlSb barrier and GaSb layers by tunneling and scattering into the conduction band of the next injection region because of a strong spatial interband coupling (a unique feature of type-II heterostructures). They are then ready for the next interband transition, which leads to sequential photon emission with a quantum efficiency possibly greater than the conventional limit of unity.

Lasing was observed [18] from 1.2 mm long stripes with 40 μm wide top ohmic contacts. The facets were uncoated, and the stripes were indium-soldered to the heat sink with the epitaxial side up. However, the material of this initial laser sample was not good; line defects emanating from the substrate cut across the stripes. Despite these defects, stimulated emission from the device was observed at temperatures up to 170 K. Fig. 3 shows the high-resolution lasing spectra at 80 and 120 K, at a repetition rate of 1 kHz and a pulse length of 100 ns. A couple of longitudinal modes could be resolved at wavelengths of 3.79–3.8 μm. The lasing threshold current (density) at 80 K was 2 A (4.17 kA/cm^2). Owing to poor material quality, this IC laser burned out shortly after lasing and did not exhibit the high differential quantum efficiency that was expected from the cascade process.

To examine the IC process, two groups of long wavelength (~ 6–8 μm) IR light-emitting diodes (LEDs) were designed by varying the number of cascade stages. Each group consisted of two samples grown in succession with the same parameters except for the period number of the active regions. The LEDs from the same group of samples displayed similar EL spectra that peaked at the same wavelength though they contained different periods of active regions. An approximate proportional relation between their differential quantum efficiencies and the period numbers of active regions was observed [19]. This scaling is associated with the sequential emission of photons as injected electrons cascade down each stage of the energy staircase structure, and it provides a direct experimental confirmation of the IC process.

The attained output power from type-II IC LEDs is

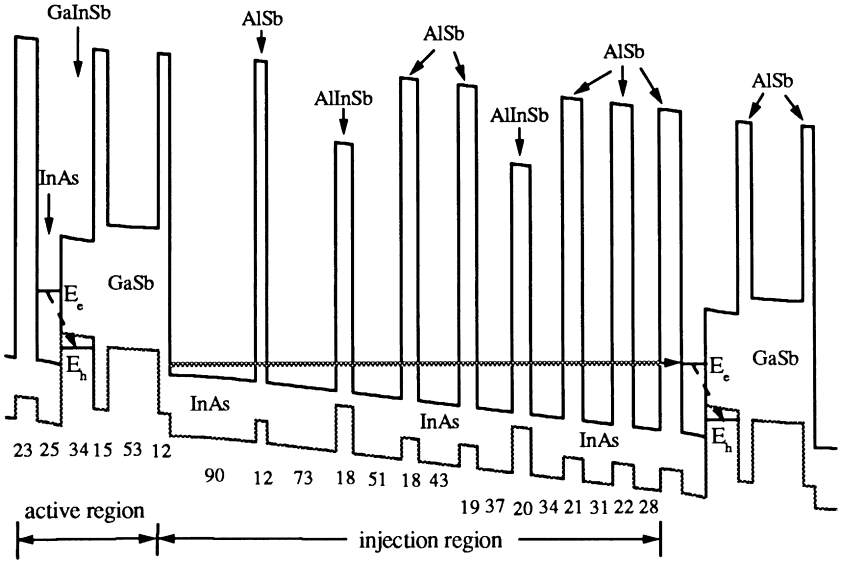

Fig. 4. Schematic band edge profile for the active and injection regions of an interband cascade laser. Numbers indicate the layer thickness (in Å). The alloys are $Ga_{0.7}In_{0.3}Sb$ and $Al_{0.7}In_{0.3}Sb$.

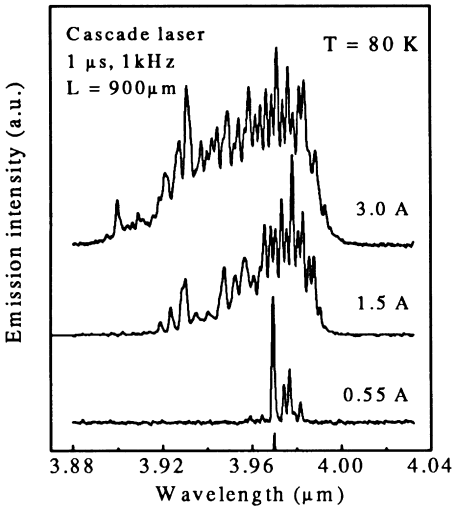

Fig. 5. High-resolution lasing spectra from a 0.2 mm wide gain-guided interband cascade laser at 80 K and at different current injection levels.

considerably higher than the maximum power reported for intersubband QC LEDs; this indicates an improved radiative efficiency as projected by the use of interband transitions to suppress the phonon scattering loss. Also, emission wavelength from IC devices at room temperature has been extended to 15 μm [20], the longest ever reported in any compound semiconductor LED for room-temperature operation. This demonstrates the unique capability of this Sb-family type-II heterostructure material system to be tailored over a wide spectral range.

3. Improved performance of interband cascade lasers at ~4 μm

3.1. Cascade layer structure

Following the preliminary characterization and demonstration of IC devices, an IC laser was designed with more careful consideration of carrier transport and grown on a *p*-type GaSb substrate. Double-crystal X-ray diffraction (DCXRD) was used to evaluate the quality of the epitaxial layers. Many sharp satellite peaks were observed from the DCXRD spectrum for this laser sample, which are indicative of its high structural quality. This IC laser structure comprises 23 repeated periods of active regions, separated by *n*-type doped-injection regions, that form the waveguide core, which is ~ 1.6 μm thick. Two *n*-type InAs/AlSb superlattices (24.3/23 Å) were employed as top and bottom optical waveguide cladding layers, with thickness of ~ 1.6 and 2 μm, respectively. Digitally graded multi-QW regions were inserted as transitional bridges for smoothing carrier transport between the waveguide core and the cladding layers, and between the cladding and the contact layers.

A detailed layer structure of one cascade period is shown in Fig. 4. Owing to the difficulties in growing an analog-graded band gap AlInAsSb layer, digital-graded band gap QWs were employed for the injection region, which serves both as a collector for the proceeding active region and as an emitter for the following one. In the injection region, all the InAs layers (except the first one, i.e. 90 Å InAs QW) were Si-doped at 6×10^{17} cm^{-3}, while the Al(In)Sb layers were undoped. The inclusion of AlInSb layers in the injection region makes the entire period strain-balanced and lattice-matched to the GaSb substrate. The injection region in the IC lasers is relatively long and has many interfaces, which could cause substantial loss due to interface roughness and scattering, and adds difficulties to achieving smooth carrier transport through the whole region. In addition, the first InAs QW of an injection region could be wider than what is needed so that the energy difference between the electron transition level in the proceeding active region and the electron level in the collector is substantially larger than the emitting photon energy. Consequently, the applied bias voltage may not be well utilized, leading to unnecessary power consumption and heating. In some early designs, a longer injection region (e.g. 815 Å long, comprising 15 QWs) was suggested [21]. Among those implemented with the long injection region, only one device lased up to 70 K [22]. Its injection region was actually shorter than the designed length due to the decrease of the growth rate. However, to avoid the dielectric breakdown of materials due to a very high electric field, the injection region should not be too short. Therefore, an appropriate balance between the above distinct aspects needs to be carefully considered in the design of injection regions and examined in the device implementation.

3.2. Laser characteristics

The laser sample was processed into broad-area gain-guided stripes with several different widths and was cleaved to cavities from about 0.5–2 mm long with uncoated facets. The lasers were then mounted epilayer-up on the temperature-controlled cold-finger of a cryostat and were electrically pumped with current pulses that ranged from 1 to 10 μs at repetition rates of 1–20 kHz. The optical output power was measured with either an InSb detector together with a digital oscilloscope or a calibrated thermopile power meter when the average power was high. In most measurements, neutral density filters were used to avoid saturating the detector.

The lasing spectra were obtained by focusing the optical output beam onto a 0.5 m monochrometer using *f*/4 optics. High-resolution lasing spectra of a laser at 80 K under different current injection levels are shown in Fig. 5. At a high injection current, the lasing spectrum shows multi-longitudinal modes and its longitudinal mode separation (24 Å) is in good agreement with the calculated value (25 Å) for the Fabry–Perot cavity. Unlike conventional lasers where a single primary mode dominates at an injection current substantially above the threshold, the lasing

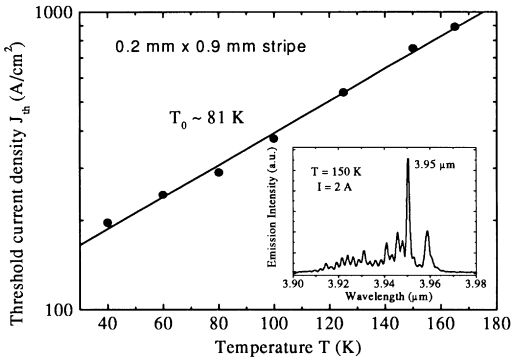

Fig. 6. Threshold current density vs heat-sink temperatures for a 0.2 mm wide gain-guided interband cascade laser. Inset is a high-resolution lasing spectrum at 150 K.

spectrum of this IC laser became even broader when it was pumped at the maximum level (3 A) of the current source used in the experiment. The laser exhibited lasing at temperatures up to 170 K [23]. In Fig. 6, the threshold current density J_{th} for a 0.2 mm wide laser with a cavity length of 0.9 mm is plotted as a function of temperature, which was considerably lower than the previously reported values in cascade lasers. For example, this laser has a threshold current density ~ 0.29 kA/cm^2 at 80 K, which was more than one order of magnitude lower than the previously achieved value (~ 4.17 kA/cm^2 at 80 K) for the first type-II IC laser. The characteristic temperature T_0 was about 81 K, partially due to more current spreading in gain-guided lasers at low temperatures.

The lasing wavelength varies in the range from 3.85 to 3.98 μm depending on the operating temperature, driving current, and devices with different threshold current densities. In comparison with the lasing spectra at 80 K, a blue shift is observed with an increase in temperature, as one can see from the lasing spectrum at 150 K shown in the inset of Fig. 6, probably because of more band filling at the higher temperature. Given the uncertainty in the growth rate and the sample uniformity, the band filling effect, as well as the nature of the spatially indirect transition in type-II QWs, the lasing wavelength agrees reasonably well with the designed value (~ 3.8 μm at 77 K).

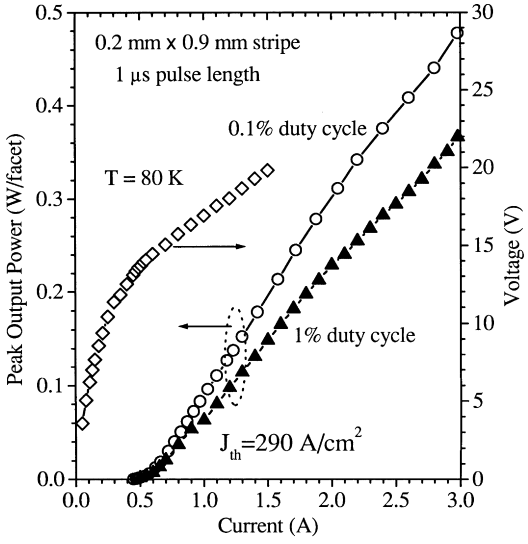

Fig. 7. Peak output power at 80 K for a broad-area gain-guided laser at pulse repetition rates of 1 kHz (circle) and 10 kHz (triangle) and its current–voltage characteristics.

Fig. 7 shows the current–voltage characteristics and the peak output power at 80 K for this laser at pulse repetition rates of 1 kHz (0.1% duty cycle) and 10 kHz (1% duty cycle), respectively. The threshold voltage was about 14 V, which is relatively high due to the larger series resistance in contrast to intersubband QC lasers. The attained peak output power was nearly 0.5 W/facet at 0.1% duty cycle with a slope of $dP/dI = 211$ mW/A, corresponding to a differential external quantum efficiency of 131% ($\sim 5.7\%$ per period), assuming two identical facets. This means that each injected electron can generate an average of ~ 1.3 emitted photons. At a 1% duty cycle, the attained peak output power was about 0.37 W/facet with a slope of $dP/dI = 155$ mW/A, which corresponds to a differential external quantum efficiency of 96% ($\sim 4.2\%$ per period). The decrease of the peak output power at the larger duty cycle was attributed to more heating. However, the attained peak output powers were the highest among interband diode lasers at this wavelength and were limited by the current source used in the experiment, as there was no saturation of the peak output power observed at the maximum drive current (3 A).

To achieve higher average power, this laser was operated with 5–10 μs long pulses at 10% duty cycles. Fig. 8 shows the peak output power per facet from this device with 5 μs long pulses at 10% duty cycle and different heat-sink temperatures. Average power up to 20 mW at 60 K (15 mW at 80 K) was achieved. The output power decreased as the heat-sink temperature increased.

To reduce current spreading, mesa structures were formed on the lasers through wet chemical etching. The peak output power per facet versus injection current from a 0.43 mm long and 0.2 mm wide mesa-structure device, electrically pumped with 1 μs long pulses at a 1 kHz repetition rate, is plotted in Fig. 9. One can see from the figure that there is substantial improvement in both the threshold current density and the quantum efficiency. At 80 K, a slope efficiency of 334 mW/A was achieved, corresponding to an external quantum efficiency of 214%, assuming equal emissions from both facets. The characteristic temperature T_0 was about 46 K, as shown in the inset of Fig. 9 for the mesa stripe IC lasers. The external quantum efficiency at 140 K dropped substantially, but was still higher than 100%. The device has lased at temperatures up to 182 K [24,25].

Several 375 μm wide mesa lasers with different cavity lengths were operated with 5 μs long pulses at a 10% duty cycle. At 80 K, all lasers exhibited similar threshold current densities (~ 110–130 A/cm^2) as shown in Fig. 10, and a

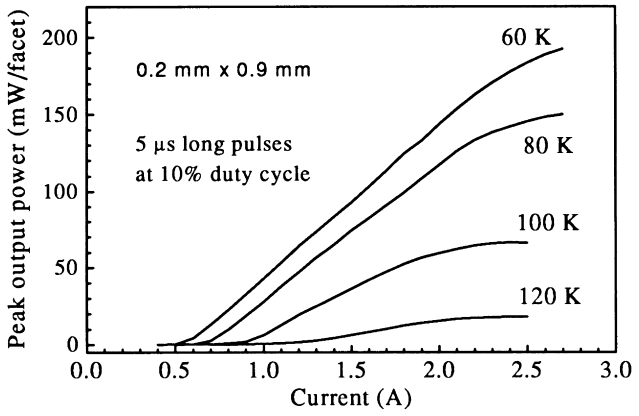

Fig. 8. Peak output power for a gain-guided laser (0.2 mm × 0.9 mm) electrically pumped with 5 μs long pulses at 10% duty cycle.

peak output power of more than 160 mW per facet was obtained, corresponding to more than 16 mW average power. The dependence of the inverse external quantum efficiency on cavity length is also plotted in Fig. 6, from which an internal quantum efficiency of 220% and an internal loss of 14 cm^{-1} were determined for these diode lasers [24,25]. Based on this estimated internal loss and the mirror loss, the slope d*P*/d*I* should be as high as ~1.6 W/A for a 1 mm long 23 period IC laser with diminishing leakage current. This high slope corresponds to an external quantum efficiency of ~10, indicating a large potential for improvement.

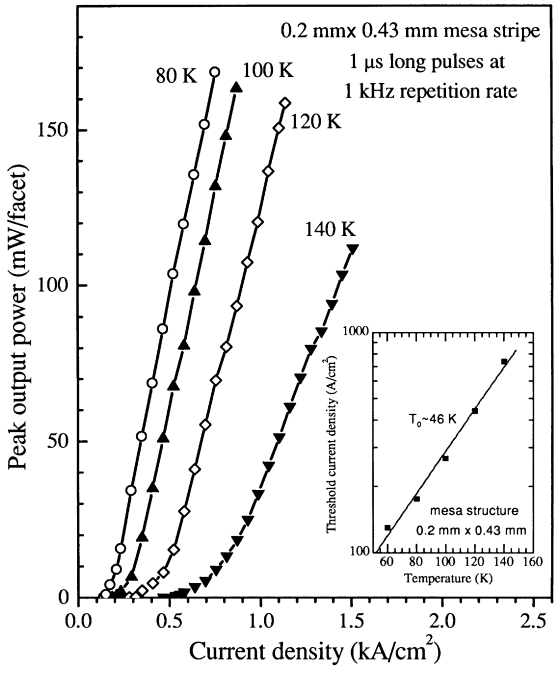

Fig. 9. Peak output power (inset: threshold current density) for a 0.2 mm wide mesa-structure laser electrically pumped with 1 μs long pulses at a 1 kHz repetition rate.

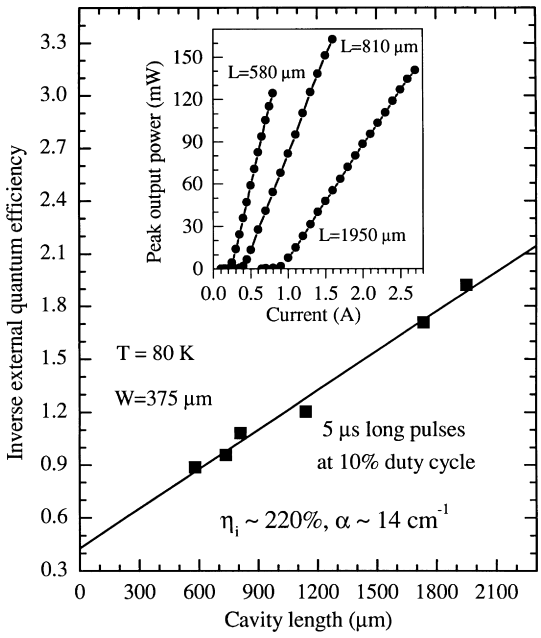

Fig. 10. Inverse external quantum efficiency vs the cavity length for 375 μm wide mesa-structure IC lasers at 80 K. Inset shows the peak output power from a single facet for three lasers.

3.3. Modeling

As there is a strong spatial interband coupling in Sb-based type-II cascade laser structures, Kane's eight-band **k·p** model [26] with an envelope wave function approximation (EFA) is adopted to account for the coupling between the conduction and valence bands in the same framework. The strain effects [27–29], up to the second order in **k** are included. The resulting 8 × 8 **k·p** Hamiltonian matrix for envelope wave functions is solved with the standard EFA boundary conditions [30] by the finite element method [31–33]. The subband dispersions along the (11) direction are shown in Fig.11 for the AlSb/InAs (25 Å)/GaInSb (34 Å)/AlSb QW active region under a constant electric field *F* of 75 kV/cm. The states are double-degenerated at zero in-plane wavevector, but spin-splitting occurs when the in-plane wavevector $k_{\|}$ has a finite value due to the asymmetric band edge profile [34,35] in type-II QWs. The separations between valence subbands near the zone center are away from the resonance with the band gap, which is beneficial to suppressing nonradiative Auger recombination and reducing optical internal loss due to intervalence subband transitions. However, the intervalence subband transition energy with an appreciable wavevector is nearly resonant with the band gap as shown by the arrows in Fig. 11, which may cause a large absorption loss. On the contrary, the probability of hole occupation in the region with a large wavevector is small. In addition, the nearly band gap-resonant intervalence subband transition region may not be significant due to the anisotropy of dispersions in the valence band as shown by the three-dimensional (3D)

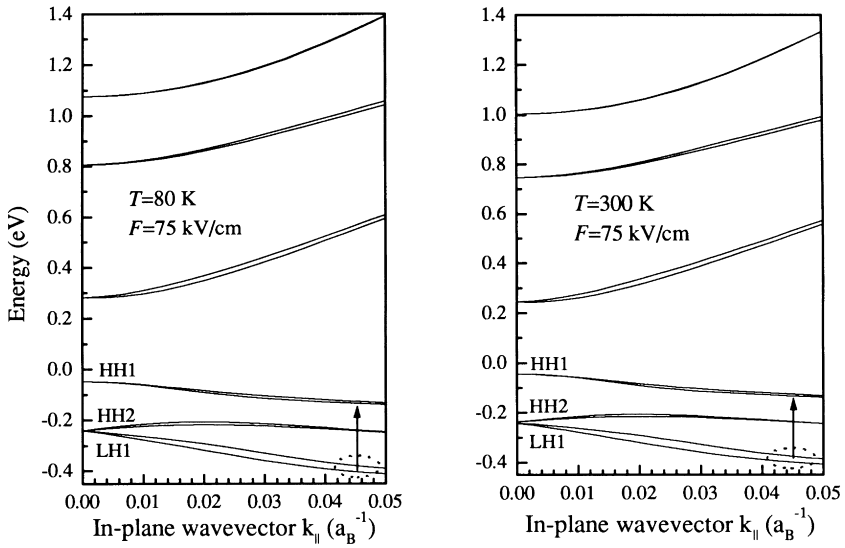

Fig. 11. Calculated subbband structures as a function of in-plane wavevector $\mathbf{k}_{\|}$ (in inverse Bohr radius) along (11) direction for the AlSb/InAs/$Ga_{0.7}In_{0.3}Sb$/AlSb QW active region under an electric field of 75 kV/cm at 80 and 300 K.

energy structure in Fig. 12 and by contour plots of constant energy for several representative subbands in Fig. 13. Those subbands have different shapes and distinct variations depending on their positions in *k*-space; Van Hove singularities are also shown in Fig. 12(b). As a result of highly anisotropic dispersions, using dispersion relations in a special direction, e.g. (10) or (11), to represent all the orientations is no longer a good approximation, and one has to evaluate the optical gain and loss according to the dispersions in all the directions of the 2D $k_x - k_y$ plane. The absorption coefficient due to intervalence subband transitions can be computed in a similar way as the gain calculation described below. As plotted in Fig. 14, the calculated absorption spectra with various 2D-hole densities (P_s) show negligible loss at the lasing photon energy. The experimentally obtained value ($\sim 14\,\mathrm{cm}^{-1}$) of the internal loss at 80 K is not large, and this supports the validity of the calculations.

In a cascade system with 2D dispersion, the dependence of the optical gain on photon energy $h\nu$ is given by

$$g(h\nu) = \alpha_{\mathrm{FS}} \frac{\lambda^2 h\nu}{n_{\mathrm{r}} m_0^2 c^2} \frac{1}{4\pi^2 L_{\mathrm{z}}} \sum_{nc} \sum_{nv} \int\int \mathrm{d}k_x\, \mathrm{d}k_y \times \frac{(\Gamma/2\pi)|M_{nv,nc}|^2 [f_{\mathrm{c}}(E_{nc}) - f_{\mathrm{v}}(E_{nv})]}{[E_{nc}(k_x,k_y) - E_{nv}(k_x,k_y) - h\nu]^2 + (\Gamma/2)^2}, \quad (1)$$

where $\alpha_{\mathrm{FS}} = \mathrm{e}^2/(\hbar c) \approx 1/137$ is the fine structure constant, n_{r} is the refractive index, E_{nc} is the energy of the *n*th electron state in the conduction band, E_{nv} is the energy of the *n*th hole

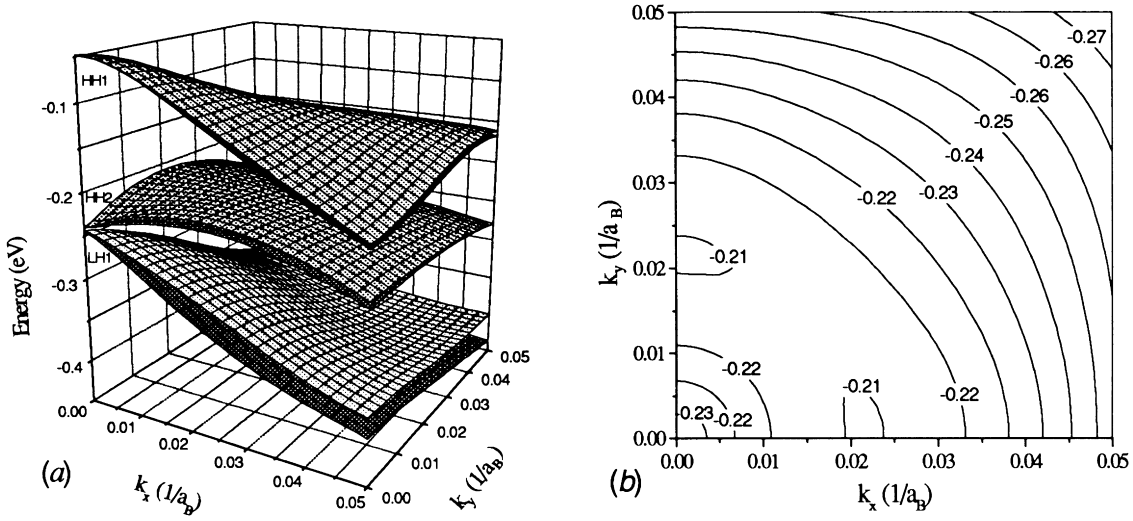

Fig. 12. (a) Subband dispersions in the valence band of the InAs/GaInSb QW active region at 300 K. (b) Two-dimensional contour plots of the subband HH2 in InAs/GaInSb QW active region at 300 K.

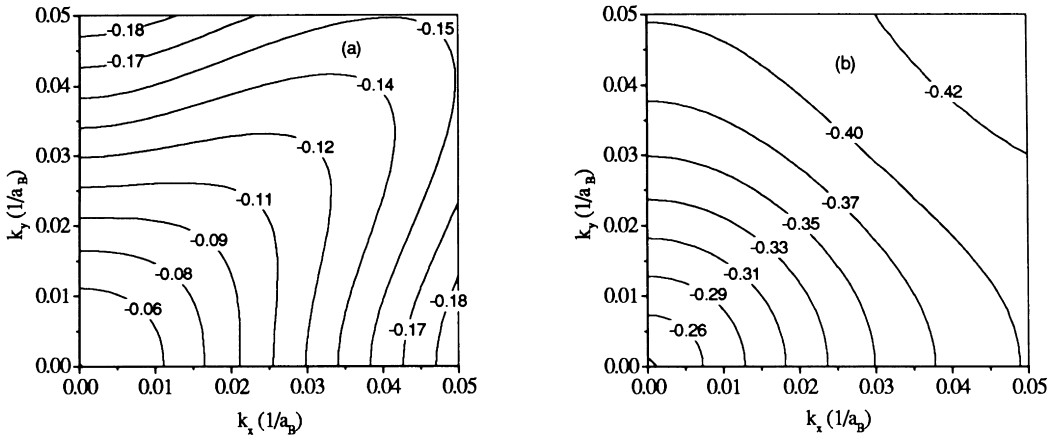

Fig. 13. Two-dimensional contour plots of the hole subbands (a) HH1 and (b) LH2 in the InAs/GaInSb QW active region at 80 K.

state in the valence band, $f_i(E)$ is the Fermi distribution function with the quasi-Fermi energy E_{Fi}, L_z is the cascade period thickness, and $M_{n,n}$, is the momentum matrix element between the nth and n'th states, which is calculated based on the general expression described by Chang and James [36] and Szmulowicz [37]. Here, a Lorentzian line-shape function with $\Gamma = 10$ meV is assumed to account for collision-broadening effects. The quasi-Fermi levels E_{Fc} and E_{Fv} are related to the injecting electron density N_s and hole density P_s.

Based on the band structures shown above, the optical gain is calculated at various injecting electron densities by assuming charge neutrality in the QW active region. Peak material gain g_{max} is plotted as a function of the injecting electron 2D density N_s in Fig. 15 [38]. As expected, in contrast to the type-I conventional laser structure, the gain saturates at a substantially lower value in the type-II cascade structures because of a relatively smaller wave function overlap (~ 0.3 here) and the lower active filling factor (as the active regions are separated by a relatively long injection region). However, it is still higher than 150 cm^{-1} at an injecting carrier density below 2.5×10^{12} cm^{-2}, which could surpass the possible optical loss for achieving lasing at room temperature. Using the experimental value of waveguide loss (14 cm^{-1}) and the calculated optical confinement factor of 0.73, one can obtain from Fig. 15 that the threshold carrier density N_{th} is 3.3×10^{11} cm^{-2} for a 1 mm long cascade laser at 80 K. At such a threshold carrier density, one should not expect a large Auger loss. Adopting an Auger coefficient $\gamma_3^{2D} = 4.5 \times 10^{-15}$ cm^4/s for an Sb-based type-II QW system [21], even though much smaller values have been predicted for optimized structures [39], the

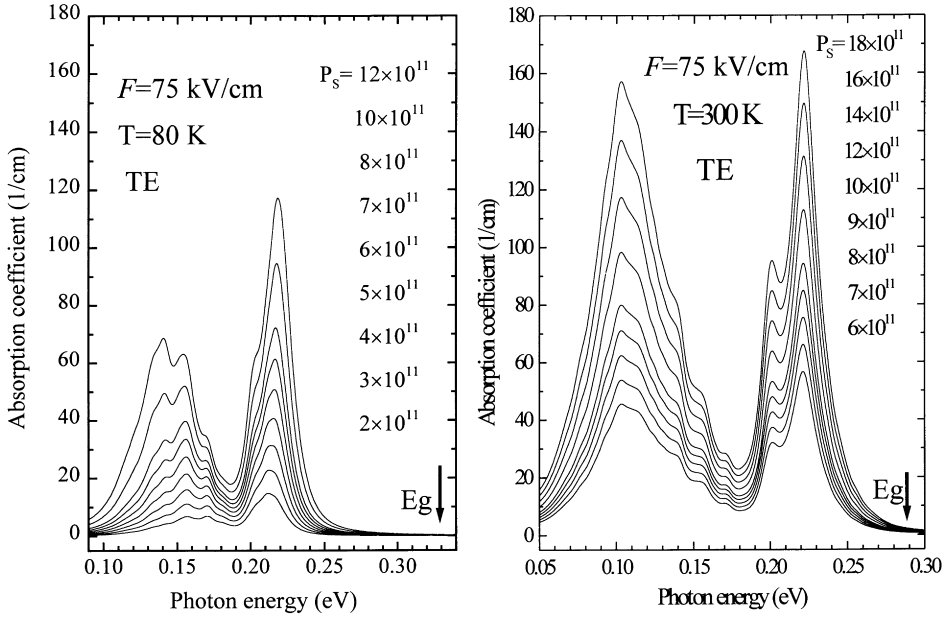

Fig. 14. Absorption coefficient as a function of the photon energy due to intervalence subband transitions at 80 and 300 K with various hole densities (P_s). Arrows indicate the band gap (E_g) position.

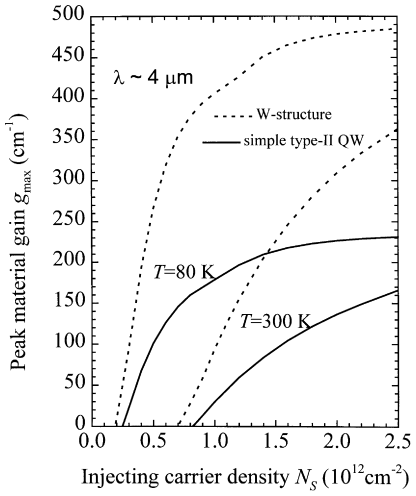

Fig. 15. Peak material gain vs injecting carrier density in IC lasers (solid curves: simple type-II QW; dotted curves: W-structure) at 80 and 300 K.

Auger recombination current density $J_A(= e\gamma_3^{2D}N_{th}^3)$ is 26 A/cm^2 at threshold. In addition, the calculated radiative current density is about 3 A/cm^2 at 80 K. Finally, the escape time due to direct tunneling from the InAs QW in the active region to the adjacent injection region is estimated to be 8 ns, resulting in a leakage current of ~ 7 A/cm^2. Summing up the three parts, we obtain a threshold current density J_{th} of ~ 36 A/cm^2, which is much smaller than the experimentally observed value (≥ 110 A/cm^2 at 80 K). This indicates that there are additional current leakage channels that may be related to interface scattering and material defects as observed in type-II cascade devices by transmission electron microscopy [19]. Furthermore, this suggests significant room for improving the performance of type-II IC lasers.

Assuming a net loss of 52 cm^{-1} for the lasing threshold at 300 K [21], the threshold carrier density is about 1.3 × 10^{12} cm^{-2} at 300 K; this results in a calculated threshold current density of ~ 1.6 kA/cm^2 due mainly to a short Auger recombination time (~ 0.13 ns) at 300 K. If the same percentage of leakage (~ 70%) due to interface scattering and defects at 80 K is assumed, the threshold current density actually required at 300 K would be over 5 kA/cm^2. Considering a relatively high threshold voltage (~ 14 V) in the type-II interband cascade lasers, the dissipated power density at 300 K is greater than 70 kW/cm^2 for achieving threshold; this results in considerable heat and makes lasing hardly achievable at room temperature. Thus, suppression of leakage current and a reduction of the threshold carrier density by the use of improved material quality and device design will be critical for room-temperature operation.

One can see from Fig. 15 that the differential gain dg_{max}/dN_s differs significantly at 80 and 300 K. This means that far more carriers are needed after the transparency point to achieve a threshold gain at high temperatures for lasing. This leads to a large increase of Auger and internal optical losses. The enhancement of the wave function overlap between two transition states would increase the differential gain and, consequently, lower the threshold carrier density. One approach is the utilization of a so-called W-active-region as reported by Felix et al. [40–43]. For the comparison, the calculated results of the peak gain in a AlSb/InAs(23 Å)/GaInSb(34 Å)/InAs(20 Å)/AlSb W-structure is also shown in Fig. 15. One can see that the gain is larger in the W-structure, and this results in a reduced threshold carrier density (2.4 × 10^{11} cm^{-2} at 80 K and 9.4 × 10^{11} cm^{-2} at 300 K), particularly at room temperature. Thus, the W-active-region IC lasers may achieve substantially improved performance at high temperatures. However, at low temperatures (e.g. 80 K), where internal losses are relatively low, the differential gain is high and the additional carrier density required after passing the transparency point for reaching the threshold gain is small. Considering that loss might increase due to more interface scattering and that the Auger recombination coefficient could also be increased due to the enhanced wave function overlap, the W-active-region IC lasers may not have better performance at low temperatures.

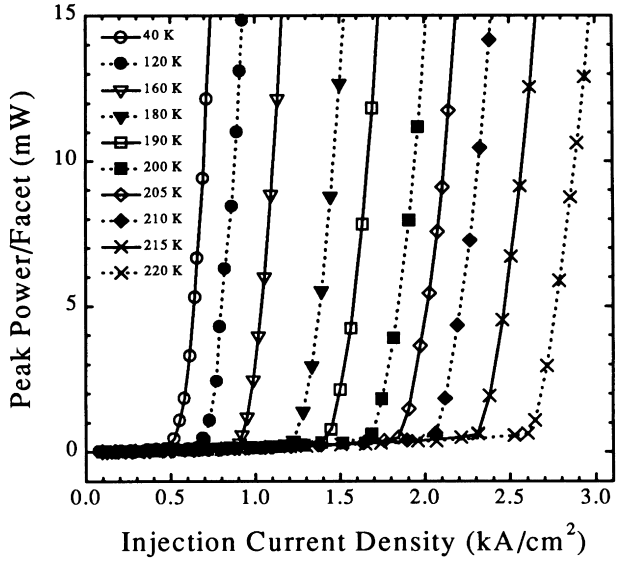

Fig. 16. Peak output power vs injection current density from a 0.14 mm wide gain-guided laser at a series of temperatures between 40 and 220 K.

4. W-active-region interband cascade lasers

The W-active-region IC lasers [40–43] were grown in the same Riber 32 MBE system as mentioned earlier on a *p*-type GaSb substrate. The first one, emitting at wavelengths of about 3 μm, comprises 22 cascade stages. Its structure is similar to the IC laser as shown in Fig. 1, but contains an additional InAs QW inserted between the GaInSb and AlSb layers in each active region. In this manner, the wave function overlap between two interband transition states is enhanced and, thus, the optical gain is increased.

The laser sample was processed into broad-area

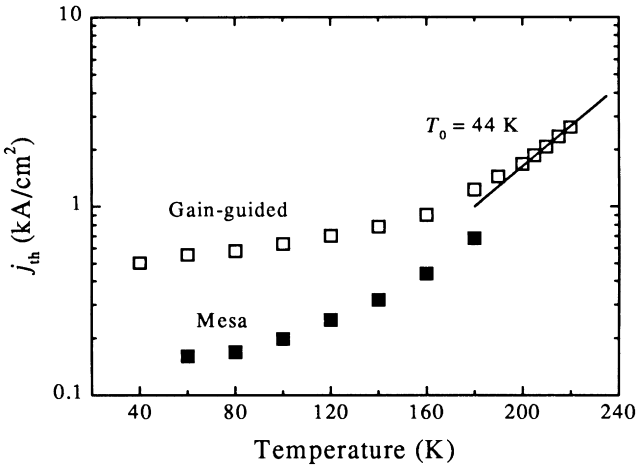

Fig. 17. Threshold injection current density vs temperature for a 140 μm wide gain-guided laser (cavity length, 1.75 mm) and a 170 μm wide mesa-structure laser (cavity length, 1.6 mm).

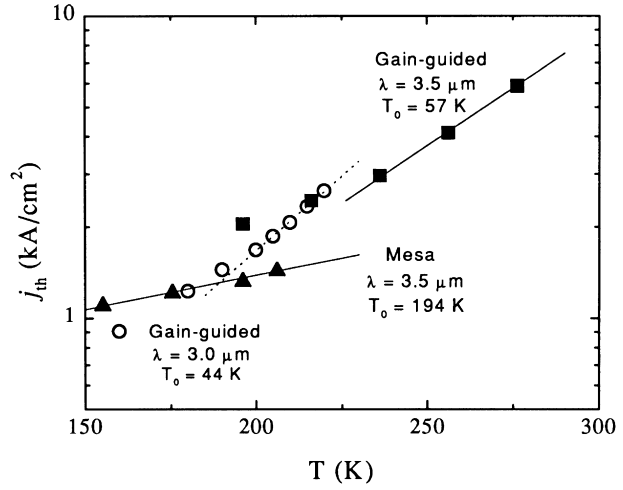

Fig. 19. Threshold current density vs temperature for the lasers emitting at 3.0 and 3.5 μm. Results are presented for gain-guided devices at each wavelength (cavity lengths of 0.5 and 0.75 mm, respectively) and a mesa-structure laser at 3.5 μm (cavity length, 0.56 mm).

gain-guided and mesa-structure devices. The laser bars were cleaved to cavity lengths L of 0.5–1.75 mm with both facets left uncoated. The lasers were electrically pumped with 100 ns long pulses at 20–200 Hz repetition rates and monitored by an InSb detector [40–43]. Fig. 16 shows the optical output power versus current density for a 140 μm wide gain-guided laser bar with a 1.75 mm long cavity at a series of temperatures between 40 and 220 K. The increase of the threshold current density jth with increasing temperature T is gradual. The plot of jth as a function of T in Fig. 17 (open points) indicates that the characteristic temperature T_0 is 230 K for $T \leq 150$ K and 44 K for $T \geq 200$ K. Lasing was obtained up to 225 K, which was limited by the onset of permanent damage whenever the injection current density exceeded ~ 2.5 kA/cm^2. With a mesa structure to suppress current spreading, the threshold current density is significantly reduced as shown also by the filled points in Fig. 17. For example, at 80 K, the threshold current density

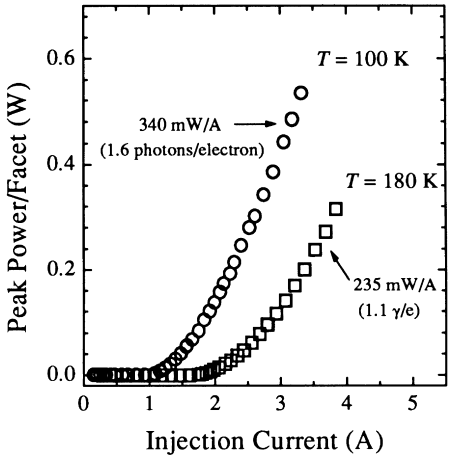

Fig. 18. Peak output power per facet vs injection current for 0.14 mm wide gain-guided lasers with a 0.5 mm long cavity at 100 K and 0.75 mm long cavity at 180 K.

for a 1.6 mm long and 170 μm wide mesa-structure laser is 170 A/cm^2, in contrast to 600 A/cm^2 for the gain-guided laser. At 180 K, the difference of their threshold current densities is still over a factor of two.

Besides the gradual increase of the threshold current density with increasing temperature, the slope efficiency was found to be weakly dependent on the temperature as shown in Fig. 16. In addition, the slope efficiency, dP/dI, continued to increase with current until damage occurred. This is apparent from the L–I curves of the gain-guided laser in Fig. 18, which shows the peak output powers when injection currents are increased up to the damage point for one device at 100 K and a second device at 180 K. Peak output powers up to 532 mW per facet at 100 K and 315 mW per facet at 180 K were obtained, the highest ever reported at each temperature for interband mid-IR lasers emitting beyond 2.9 μm. At the highest injection levels, the slopes were 342 mW/A per facet at 100 K and 235 mW/A per facet at 180 K. Assuming identical emission from two facets, these values correspond to an external quantum efficiency of 1.6 photons at 100 K and 1.1 photons at 180 K, respectively, as an average generated per electron injected.

The second W-active-region IC laser structure is similar to the first W-active-region IC laser, but contains an additional hole QW ($Ga_{0.7}In_{0.3}Sb$) followed by GaSb and AlSb layers in each active region [40–43]. This was done in an attempt to minimize the leakage from the two InAs QWs in the active region to the injection region. This laser, comprising 25 cascade stages, was designed to have the same active region as the first one ($\lambda \sim 3$ μm) but with a shorter injection region. However, the observed lasing wavelength was about 3.5 μm [40–43] as the MBE growth actually deviated somewhat from the design. The lasers, with cavity lengths L of 0.5–1 mm with both facets left

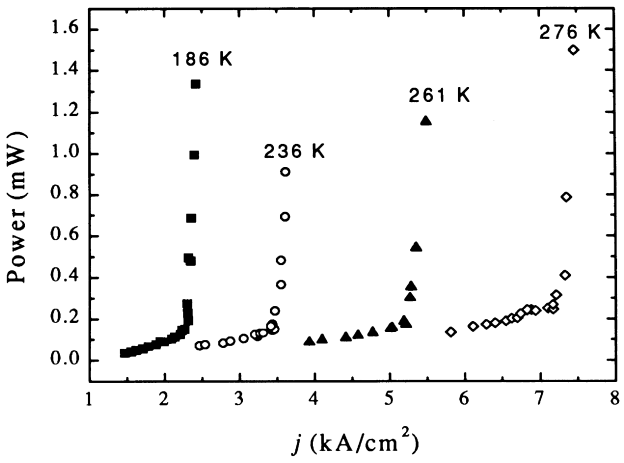

Fig. 20. Peak output power per facet for the gain-guided interband cascade laser (cavity length, 0.75 mm) emitting at 3.5 μm at several operating temperatures.

uncoated, were electrically pumped with 100 ns long pulses at 5–50 Hz repetition rates and monitored by an InSb detector.

Fig. 19 shows the threshold current density as a function of temperature for a gain-guided device (filled squares) and a mesa-structure laser (triangles) emitting at 3.5 μm, along with a gain-guided 3 μm laser (circles) from the first W-active-region IC laser wafer. For the gain-guided 3.5 μm IC laser, a characteristic temperature T_0 of 160 K was obtained for $T \leq 235$ K, while $T_0 = 57$ K for $235 < T < 276$ K, showing unusual temperature dependence in contrast to conventional mid-IR interband diode lasers. Furthermore, the slope near the threshold is comparable at 276 K to its value at 186 K, as shown in Fig. 20. A different bar from this W-active-region sample exhibited lasing at temperatures up to 286 K, which was also limited by the onset of permanent damage at a high injection level rather than by heating.

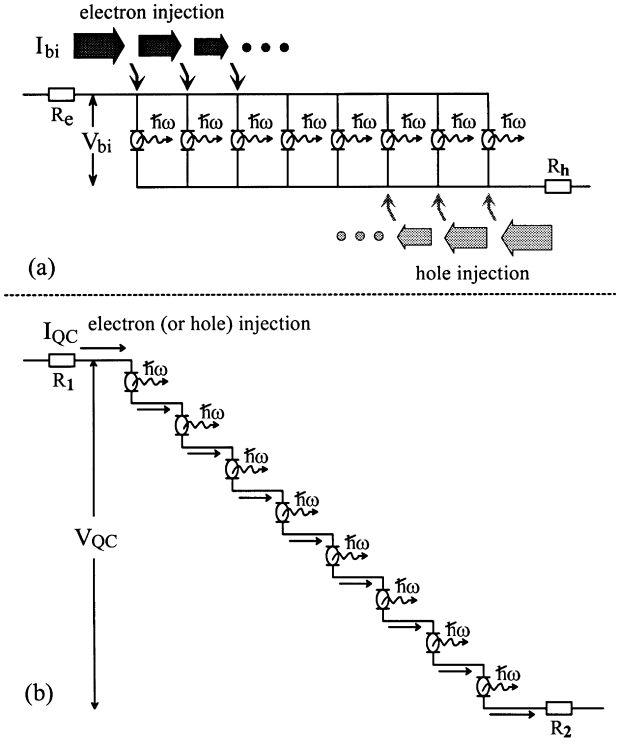

Fig. 21. Carrier transport in and equivalent circuit for (a) a conventional bipolar laser structure, and (b) a quantum cascade laser.

5. Power efficiency

In contrast to a conventional bipolar diode laser where multiple QWs in the active region are connected in parallel as shown in Fig. 21(a), QW active regions in a cascade laser structure are connected in series (Fig. 21(b)). Ideally, as a consequence, current is traded for voltage in cascade laser structures. This means that the minimal bias voltage V_0 and minimal injection current I_0 required for a desired output power $P_o = I_0V_0$ at a photon energy $E_p = h\nu$ are related to the cascade stages N_c (equal to one for noncascade configurations) as expressed by

$$V_0 = N_c V_p, \tag{2}$$

$$I_0 = P_o/(N_c V_p), \tag{3}$$

where $V_p = E_p/e$. In practice, the applied bias voltage V and the total injection current I would not exactly follow the relationship as indicated by Eqs. (2) and (3) because there is always an excess voltage ΔV and an excess current ΔI in devices. How the excess current and voltage affect the laser performance can be evaluated in terms of power conversion (wall-plug) efficiency $\eta = P_o/P_{in}$. Expressing the input power P_{in} as

$$P_{in} = IV = (I_0 + \Delta I)(V_0 + \Delta V), \tag{4}$$

one can obtain

$$\eta^{-1} = 1 + \frac{\Delta I}{I_0} + \frac{\Delta V}{V_0} + \frac{\Delta I}{I_0}\cdot\frac{\Delta V}{V_0}. \tag{5}$$

In an ideal case, $\Delta I = \Delta V = 0$, and $\eta = 1$; so no power is wasted. In practical cases where there are additional voltage drops due to parasitic resistances, leakage currents, and nonradiative processes, which result in nonnegligible excess voltage ΔV and excess current ΔI, there is always dissipated power $P_D = P_{in} - P_o = P_{in}(1 - \eta)$. The resulting heat is detrimental to the operation of the device and limits the device performance. Therefore, it is especially important to maximize power efficiency. How this is done depends on the laser structure, approach, and materials. From Eq. (5), one finds that power efficiency is completely determined by the *normalized* excess current $\Delta I/I_0$ and voltage $\Delta V/V_0$, which are more appropriate than ΔI and ΔV for describing device performance. The contours of constant power efficiency in terms of $\Delta I/I_0$ and $\Delta V/V_0$ are shown in Fig. 22. The contours can also represent the optically

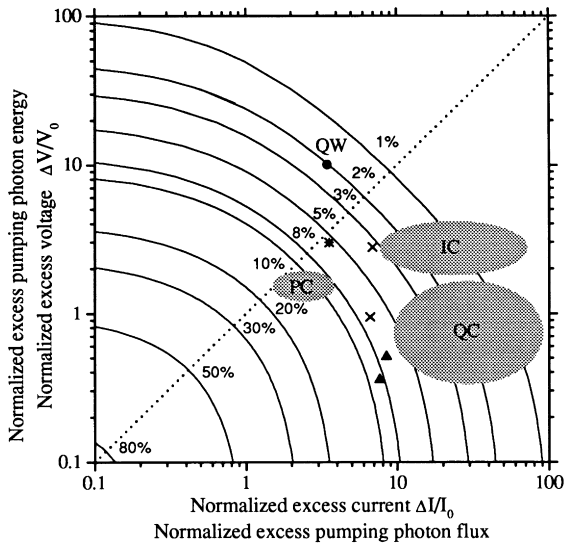

Fig. 22. Contours of constant power efficiency. The circle is for a type-I QW diode laser at 80 K [44]. The star is for a type-II QW laser ($\sim$ 3.9 μm) at 69 K optically pumped with 6 μs long pulses at 2 kHz repetition rate [45]. Crosses are for a 3.7 μm quasi-cw InAsSb type-I double-heterostructure laser at 72 K optically pumped with 1.9 and 0.98 μm diodes, respectively [46]. Triangles are for two cw QC lasers at $\sim$ 20 K [5–7], which comprise 25 ($\lambda \sim 5$ μm) and 30 ($\lambda \sim 8$ μm) cascade stages, respectively. The shaded areas (QC, IC, PC) are estimates and speculations for QC, IC, and projected optimized cascade lasers, respectively, operating at temperatures above 77 K.

pumped lasers if the normalized excess-pumping photon flux and excess-pumping photon energy $\Delta E_{\text{pump}}/E_{\text{p}}$ are used.

We can specify $\Delta I/I_0$ and $\Delta V/V_0$ as,

$$\frac{\Delta V}{V_0} = \frac{V_{\text{c}}}{N_{\text{c}} V_{\text{p}}} + \frac{\Delta V_{\text{s}}}{V_{\text{p}}} \tag{6}$$

$$\frac{\Delta I}{I_0} = \frac{I_{\text{th}} + \Delta I_{\text{l}}}{P_0/(N_{\text{c}} V_{\text{p}})} \tag{7}$$

where ΔV_{s} is the excess voltage drop due to a series resistance R_{s} in a single cascade stage, V_{c} is the voltage across the series resistance R_{c} from contacts and cladding regions, I_{th} is the threshold current, and ΔI_{l} is a leakage current increment after lasing in addition to the threshold current. Here, a small contribution of spontaneous emission to the lasing mode has been neglected in deriving Eq. (7). From Eq. (6), one can see that the voltage drop V_{c} across the series resistance R_{c} is less important due to the series stack of many active regions, which significantly reduces $\Delta V/V_0$ in a cascade structure in contrast to the conventional parallel configuration. On the contrary, $\Delta I/I_0$ can be larger in cascade structures due to smaller I_0 than that in the parallel configuration if the excess current ΔI is not scaled down accordingly in the QC structure for the reason discussed later. In Fig. 22, the dotted-line divides conventional mid-IR diode lasers and cascade lasers into two distinct groups. For example, Lincoln Lab's InAs/InAlAsSb QW laser ($\lambda \sim 3.4$ μm) [44] has a maximum cw output power of 215 mW/facet at 80 K, with a driving current I of $\sim$ 5.28 A and applied bias V of $\sim$ 4 V. One can find that $\Delta I/I_0 \sim 3.48$, $\Delta V/V_0 \sim 9.97$, leading to $\eta \sim 2\%$ with $P_{\text{D}} \sim 20.7$ W.

For intersubband QC lasers, the series resistance R_{s} in an active region is very small, owing to fast phonon scattering. This results in a small excess voltage ΔV_{s}, and $\Delta V/V_0$ less than one, so that $\Delta I/I_0$ is the leading term for heat generation. Because of a high threshold current density, $\Delta I/I_0$ is usually larger than 10 at a temperature above 77 K; this limits the power efficiency to no higher than 10%. However, due to a very small $\Delta V/V_0$, the power efficiency of QC lasers (e.g. $\sim$3.5% at 80 K [5–7]) can be higher than what has been achieved in conventional mid-IR diode lasers, and comparable to efficiencies obtained in optically pumped mid-IR semiconductor lasers [45,46] as shown in Fig. 22.

In type-II IC lasers, due to a relatively larger series resistance in the active region, the applied voltage is not utilized as efficiently as in intersubband QC lasers and $\Delta V/V_0$ has values of about 2 to 3, which can be lowered somewhat by reducing contact resistance and with improved design. However, the present IC lasers also have a very large excess current with $\Delta I/I_0 > 10$. This results in a power efficiency smaller than what intersubband QC lasers can achieve (Fig. 22), though the observed threshold current densities of IC lasers at low temperature are significantly smaller than those in intersubband QC lasers. So far, the observed threshold current densities (> 100 A/cm^2 at 80 K) of IC lasers are higher than what can be reached from conventional type-I interband diode lasers (e.g. 78 A/cm^2 at 80 K [47]). The relatively high threshold current density in present IC lasers is due to a dominant leakage current ($\sim$ 70–90%) associated with material defects, tunneling, and thermionic emissions. Owing to a large leakage current, the threshold current density in IC lasers is comparable to that in the conventional parallel configuration [48,49], and could not be scaled down as suggested by the ideal trade off between the voltage and current, which would lead to a $\Delta I/I_0$ larger than that in conventional parallel laser structures. With improved material quality and design, leakage current in the IC lasers may be reduced so that their power efficiency can be raised to the projected area as shown in Fig. 22.

The other aspect that needs to be explored is the dependence of power efficiency on the number of cascade stages. To examine this issue, we come back to discuss the implications of Eqs. (6) and (7). I_{th} can be further specified as

$$I_{\text{th}} = \text{e}(n_{\text{tr}} + \Delta n)/\tau, \tag{8}$$

where n_{tr} is the transparency carrier density, Δn is an additional carrier density required after the transparency point for reaching the threshold, and τ is a transit/life time due to various mechanisms including leakage and radiative and nonradiative relaxation processes. Essentially, in QC lasers, n_{tr}, τ, and ΔI_{l} do not depend on the number of cascade

stages, while Δn does. However, for QC lasers without large optical loss, as differential gain is high in QW structures particularly at low temperatures, Δn is smaller than n_{tr}, resulting in a weak dependence of ΔI on the number of cascade stages. In cascade lasers, $\Delta V/V_0$ decreases with the number of cascade stages and approaches a saturation value of $\Delta V_s/V_p$ as shown in Eq. (6). Thus, less benefit can be gained for minimizing $\Delta V/V_0$ by further increasing cascade stages over a certain number. This is also true for increasing the output power P_o due to a nonuniform distribution of the optical field in the waveguide. Thus, $\Delta I/I_0$ may become larger by increasing the number of cascade stages when the excess current ΔI is not scaled down accordingly. This leads to a nonmonotonic dependence of power efficiency on cascade stages. Lasers with varying cascade stages and separate optical confinement structures could be designed to examine such dependence.

6. Concluding remarks

Type-II interband cascade lasers have been demonstrated as a new type of mid-IR light source with large peak output powers, high differential external quantum efficiencies ($>$ 200%), and near-room-temperature operation (286 K). The output power and the maximum operating temperature in the IC lasers, especially with the mesa structures, were limited by the damage at high injection levels before saturation. Possible causes of the damage include material defects and high electric fields typical in cascade structures. Certainly, the type-II IC lasers are still in an early stage of development and are far from optimum. Besides the material quality, there may also be many other issues in device design, such as carrier transport, nonradiative processes, internal absorption losses, and their interplay, which could substantially affect the laser performance. Considering that the Sb-based material system and heterostructures have been much less investigated in contrast to GaAs- and InP-based compound semiconductor systems, the preliminary results of IC lasers are especially stimulating. Our analyses and modeling also suggest significant room to improve the performance of IC lasers. Besides, numerous variations of type-II cascade laser structures with other materials and their combinations are possible, which should provide flexibility and opportunities. Very recently, intersubband electroluminescence ($\lambda \sim 6\ \mu m$) was observed [50] from type-II cascade structures based on InAs/GaSb/AlSb QWs that made use of the band gap blocking feature [51–54] in type-II heterostructures. With continued and extensive efforts to improve the material quality and deepen our understanding of the underlying physics, Sb-based type-II interband cascade lasers promise to meet the requirements of many applications.

Note added in proof

IC lasers based on type-II QWs were recently grown and demonstrated at the US Army Research Laboratory. This successful growth at a second laboratory (University of Houston was the first) illustrates the fact that these type-II IC lasers should be relatively straightforward to grow at any good MBE facility.

Acknowledgements

The work described was carried out in collaborations with A.A. Allerman and S.R. Kurtz of Sandia National Laboratories; W.W. Bewley, C.L. Felix, J.R. Meyer, I. Vurgaftman and their colleagues of NRL; M. Buchanan, E. Dupont, H.C. Liu, and J.P. McCaffrey of NRC of Canada; P.C. Chang, C.-H. Lin, Y.-M. Mu, S.J. Murry, B. Yang, and D. Zhang of the University of Houston; The research at the University of Houston was partially supported by NASA under Cooperative Agreement-NCC8-127, TcSUH, and QET Inc. The work at QET was partially supported by the Ballistic Missile Defense Organization/Innovative Science and Technology, and managed by the Avionics Directorate of Wright Laboratory (K.L. Schepler), Aeronautical Systems Center, USAF Wright-Patterson AFB OH 45433 with contract No. F33615-96-C-1904, and the Office of Naval Research (L.R. Cooper) with contract No. N00014-97-C-0259. This review was completed while the author held a National Research Council/ARL Senior Research Associateship. The author is grateful to W.J. Woodbridge and D.E. Wortman for their constructive comments and careful reading.

References

[1] J. Faist, F. Capasso, D.L. Sivco, C. Sirtori, A.L. Hutchinson, A.Y. Cho, Science 264 (1994) 553.
[2] L. Esaki, R. Tsu, IBM J. Res. Dev. 14 (1970) 61.
[3] R.F. Kazarinov, R.A. Suris, Sov. Phys. Semicond. 5 (1971) 707.
[4] R.F. Kazarinov, R.A. Suris, Sov. Phys. Semicond. 6 (1972) 120.
[5] J. Faist, A. Tredicucci, F. Capasso, C. Sirtori, D.L. Sivco, J.N. Baillargeon, A.L. Hutchinson, A.Y. Cho, IEEE J. Quantum Electron. 34 (1998) 336.
[6] C. Gmachl, private communications, 1997.
[7] C. Gmachl, A. Tredicucci, F. Capasso, A.L. Hutchinson, D.L. Sivco, J.N. Baillargeon, A.Y. Cho, Appl. Phys. Lett. 72 (1998) 3130.
[8] R.Q. Yang, at 7th International Conference on Superlattices, Microstructures and Microdevices, Banff, Canada, August, 1994.
[9] R.Q. Yang, Superlattices and Microstructures 17 (1995) 77.
[10] R.Q. Yang, Patent Disclosure, University of Toronto, unpublished.
[11] R.Q. Yang, US Patent No. 5,588,015, 1996.
[12] J.R. Meyer, I. Vurgaftman, R.Q. Yang, L.R. Ram-Mohan, Electron. Lett. 32 (1996) 45.
[13] R.Q. Yang, S.S. Pei, J. Appl. Phys. 79 (1996) 8197.
[14] R.Q. Yang, Novel concepts and structures for infrared lasers, in: M. Helm (Ed.), Long Wavelength Infrared Emitters Based on Quantum Wells and Superlattices, Gordon and Breach, New York, 1999, in press.
[15] R.Q. Yang, C.-H. Lin, P.C. Chang, S.J. Murry, D. Zhang, S.S. Pei, S.R. Kurtz, S.N.G. Chu, F. Ren, Electron. Lett. 32 (1996) 1621.

[16] R.Q. Yang, C.-H. Lin, S.J. Murry, S.S. Pei, H.C. Liu, M. Buchanan, E. Dupont, Appl. Phys. Lett. 70 (1997) 2013.
[17] R.Q. Yang, C.-H. Lin, S.J. Murry, D. Zhang, S.S. Pei, E. Dupont, H.C. Liu, M. Buchanan, in: H.K. Choi, P.S. Zory (Eds.), In-plane Semiconductor Lasers: from Ultraviolet to Midinfrared, Proc. SPIE, 3001, 1997, pp. 282.
[18] C.-H. Lin, R.Q. Yang, D. Zhang, S.J. Murry, S.S. Pei, A.A. Allerma, S.R. Kurtz, Electron. Lett. 33 (1997) 598.
[19] E. Dupont, J.P. McCaffrey, H.C. Liu, M. Buchanan, R.Q. Yang, C.-H. Lin, D. Zhang, S.S. Pei, Appl. Phys. Lett. 72 (1998) 1495.
[20] D. Zhang, E. Dupont, R.Q. Yang, H.C. Liu, C.-H. Lin, M. Buchanan, S.S. Pei, Optics Exp. 1 (1997) 97.
[21] I. Vurgaftman, J.R. Meyer, L.R. Ram-Mohan, IEEE Phot. Tech. Lett. 9 (1997) 170.
[22] Sample was grown at UH, and fabricated and tested in NRL. J.R. Meyer, at Second Workshop on Characterization, Future Opportunities and Applications of 6.1 Å III–V semiconductors, NRL, August, 1998.
[23] R.Q. Yang, B.H. Yang, D. Zhang, C.-H. Lin, S.J. Murry, H. Wu, S.S. Pei, Appl. Phys. Lett. 71 (1997) 2409.
[24] B.H. Yang, D. Zhang, R.Q. Yang, C.-H. Lin, S.J. Murry, S.S. Pei, Appl. Phys. Lett. 72 (1998) 2220.
[25] B.H. Yang, R.Q. Yang, D. Zhang, C.-H. Lin, S.S. Pei, Proc. SPIE 3457 (1998) 324.
[26] E.O. Kane, in: R.K. Willardson, A.C. Beer (Eds.), Physics of III–V Compounds, Semiconductors and Semimetals, 1, Academic Press, New York, 1966, pp. 75.
[27] G.L. Bir, G.E. Pikus, Symmetry and Strain-induced Effects in Semiconductors, Wiley, New York, 1974.
[28] T.B. Bahder, Phys. Rev. B 41 (1990) 11 992.
[29] P. Enders, A. Barwolff, M. Woerner, D. Suisky, Phys. Rev. B 51 (1995) 16 695.
[30] F. Szmulowicz, G.J. Brown, Phys. Rev. B 51 (1995) 13 203.
[31] K. Nakamura, A. Shimizu, M. Koshiba, K. Hayata, IEEE J. Quantum Electron. 25 (1989) 889.
[32] K. Nakamura, A. Shimizu, M. Koshiba, K. Hayata, IEEE J. Quantum Electron. 27 (1991) 2035.
[33] L.R. Ram-Mohan, J.R. Meyer, J. Nonlinear Opt. Phys. Mater. 4 (1995) 191.
[34] G. Goldoni, A. Fasolino, Phys. Rev. Lett. 26 (1992) 2567.
[35] R. Winkler, U. Rossler, Phys. Rev. B 48 (1993) 8918.
[36] Y.-C. Chang, R.B. James, Phys. Rev. B 39 (1989) 12 672.
[37] F. Szmulowicz, Phys. Rev. B 51 (1995) 1613.
[38] Y.-M. Mu, R.Q. Yang, J. Appl. Phys. 84 (1998) 5357.
[39] M.E. Flatte, C.H. Grein, H. Ehrenreich, R.H. Miles, H. Cruz, J. Appl. Phys. 78 (1995) 4552.
[40] C.L. Felix, W.W. Bewley, I. Vurgaftman, J.R. Meyer, D. Zhang, C.-H. Lin, R.Q. Yang, S.S. Pei, IEEE Photonics Technol. Lett. 9 (1997) 1433.
[41] C.L. Felix, W.W. Bewley, E.H. Aifer, I. Vurgaftman, J.R. Meyer, C.-H. Lin, D. Zhang, S.J. Murry, R.Q. Yang, S.S. Pei, J. Electronic Mater. 27 (1998) 77.
[42] R.Q. Yang, C.-H. Lin, B.H. Yang, D. Zhang, S.J. Murry, S.S. Pei, W.W. Bewley, L.J. Olafsen, E.H. Aifer, C.L. Felix, I. Vurgaftman, J.R. Meyer, Proc. SPIE 3284 (1998) 308.
[43] L.J. Olafsen, E.H. Aifer, I. Vurgaftman, W.W. Bewley, C.L. Felix, J.R. Meyer, D. Zhang, C.-H. Lin, S.S. Pei, Appl. Phys. Lett. 72 (1998) 2370.
[44] H.K. Choi, G.W. Turner, M.J. Manfra, Electron. Lett. 32 (1996) 1296.
[45] H.Q. Le, C.H. Lin, S.J. Murry, R.Q. Yang, S.S. Pei, IEEE J. Quantum Electron. 34 (1998) 1016.
[46] H.Q. Le, G.W. Turner, J.R. Ochoa, IEEE Photon. Technol. Lett. 10 (1998) 663.
[47] H.K. Choi, G.W. Turner, Appl. Phys. Lett. 67 (1995) 332.
[48] D.H. Chow, R.H. Miles, T.C. Hasenberg, A.R. Kost, Y.H. Zhang, H.L. Dunlap, L. West, Appl. Phys. Lett. 67 (1995) 3700.
[49] W.W. Bewley, E.H. Aifer, C.L. Felix, I. Vurgaftman, J.R. Meyer, C.-H. Lin, S.J. Murry, D. Zhang, S.S. Pei, Appl. Phys. Lett. 71 (1997) 3607.
[50] K. Ohtani, H. Ohno, Appl. Phys. Lett. 74 (1999) 1409.
[51] R.Q. Yang, J.M. Xu, Appl. Phys. Lett. 59 (1991) 181.
[52] H. Ohno, L. Esaki, E.E. Mendez, Appl. Phys. Lett. 60 (1992) 3153.
[53] R.Q. Yang, J.M. Xu, Phys. Rev. B 46 (1992) 6969.
[54] R.Q. Yang, J.M. Xu, Can. J. Phys. 70 (1992) 1153.